

University of Groningen

## 7.1 T MRI to Assess the Anterior Segment of the Eye

Langner, Soenke; Martin, Heiner; Terwee, Thom; Koopmans, Steven A.; Krueger, Paul C.; Hosten, Norbert; Schmitz, Klaus-Peter; Guthoff, Rudolf F.; Stachs, Oliver

*Published in:*  
Investigative ophthalmology & visual science

*DOI:*  
[10.1167/iops.09-4865](https://doi.org/10.1167/iops.09-4865)

**IMPORTANT NOTE:** You are advised to consult the publisher's version (publisher's PDF) if you wish to cite from it. Please check the document version below.

*Document Version*  
Publisher's PDF, also known as Version of record

*Publication date:*  
2010

[Link to publication in University of Groningen/UMCG research database](#)

*Citation for published version (APA):*

Langner, S., Martin, H., Terwee, T., Koopmans, S. A., Krueger, P. C., Hosten, N., Schmitz, K-P., Guthoff, R. F., & Stachs, O. (2010). 7.1 T MRI to Assess the Anterior Segment of the Eye. *Investigative ophthalmology & visual science*, 51(12), 6575-6581. <https://doi.org/10.1167/iops.09-4865>

**Copyright**

Other than for strictly personal use, it is not permitted to download or to forward/distribute the text or part of it without the consent of the author(s) and/or copyright holder(s), unless the work is under an open content license (like Creative Commons).

The publication may also be distributed here under the terms of Article 25fa of the Dutch Copyright Act, indicated by the "Taverne" license. More information can be found on the University of Groningen website: <https://www.rug.nl/library/open-access/self-archiving-pure/taverne-amendment>.

**Take-down policy**

If you believe that this document breaches copyright please contact us providing details, and we will remove access to the work immediately and investigate your claim.

*Downloaded from the University of Groningen/UMCG research database (Pure): <http://www.rug.nl/research/portal>. For technical reasons the number of authors shown on this cover page is limited to 10 maximum.*

## 7.1 T MRI to Assess the Anterior Segment of the Eye

Sönke Langner,<sup>1</sup> Heiner Martin,<sup>2</sup> Thom Terwee,<sup>3</sup> Steven A. Koopmans,<sup>4</sup> Paul C. Krüger,<sup>1</sup> Norbert Hosten,<sup>1</sup> Klaus-Peter Schmitz,<sup>2</sup> Rudolf F. Guthoff,<sup>5</sup> and Oliver Stachs<sup>5</sup>

**PURPOSE.** Visualization of the anterior segment and biometric evaluation of the entire crystalline lens pose significant challenges for imaging techniques because of tissue-induced distortion artifacts. The present study was conducted to demonstrate the advantages of high-resolution magnetic resonance imaging (micro-MRI) for visualizing the anterior segment.

**METHODS.** High-resolution MR ocular images were acquired on an ultra-high-field MR unit using a two-channel coil with four coil elements and  $T_2$ -weighted turbo spin echo sequences ex vivo in pig, rabbit, monkey, and human donor eyes and in vivo in rabbits. Tissue heating, reproducibility, and signal-to-noise ratio were investigated in vivo. Monkey eye lens thickness (LT) was also measured using A-scan ultrasonography (US).

**RESULTS.** Anterior segment details of phakic eyes were obtained ex vivo (pig, rabbit, monkey, and human donor eyes) with pixel matrix size  $512 \times 512$  (in-plane resolution  $80 \times 80 \mu\text{m}$ ) and in vivo (rabbit eyes) with pixel matrix size  $320 \times 320$  (in-plane resolution  $125 \times 125 \mu\text{m}$ ). Complete quantification of lens dimensions as they correlate with the sulcus-sulcus and angle-angle plane can be performed. In LT determinations in monkey eyes, no significant difference was detected between micro-MRI and A-scan US ( $P > 0.05$ , Mann-Whitney  $U$  test). Biometric analysis of one pseudophakic monkey eye confirmed the absence of relevant distortion artifacts.

**CONCLUSIONS.** Micro-MRI allows ex vivo and in vivo visualization and quantification of the spatial arrangement of the anterior eye segment. Imaging of the retroiridian region, including the entire crystalline lens, overcomes a number of major limitations in the quantitative evaluation of the anterior segment. (*Invest Ophthalmol Vis Sci.* 2010;51:6575–6581) DOI:10.1167/iovs.09-4865

Quantitative anterior segment imaging is regarded as more complex than retinal imaging because of tissue-induced distortion artifacts. In recent decades several techniques have been developed to allow objective imaging of the anterior segment<sup>1</sup>; these include ultrasound biomicroscopy,<sup>2</sup> Scheimpflug imaging,<sup>3</sup> and optical coherence tomography.<sup>4</sup> However,

all these modalities have major limitations when they are used for quantitative anterior segment evaluation. In all optical methods the iris pigment constitutes an obstacle to viewing the important structures of the lens equator.<sup>1</sup> Ultrasound biomicroscopy is vulnerable to distortion because of different sound velocities in different ocular and related media. All acoustic and light detection methods are therefore subject to image distortion by the intervening surfaces and require mathematical remodeling.<sup>1</sup>

Magnetic resonance imaging (MRI) is a valuable tool in the field of medical imaging. The eye is an ideal tissue for high-field MRI because of its wide variation in water content and in particular because of the requirement for high spatial resolution in a small field of view (FoV). MRI is currently used in ophthalmology for posterior segment imaging,<sup>5–11</sup> orbital imaging,<sup>12</sup> and anterior segment imaging.<sup>10,13–16</sup> Increasing the field strength of the static magnetic field ( $B_0$ ) results in improved signal-to-noise ratio (SNR). This is associated with enhanced spatial resolution and a shorter scanning time. Ultra-high-field MRI at 7.1 T has become an important tool in neurologic research and has already been used to visualize the human eye in vivo.<sup>17</sup> The gain in SNR makes ultra-high-field MRI suitable for imaging intraocular structures of the eye. Unlike the other imaging modalities listed above, to give true anatomic proportions, MRI relies essentially on the homogeneity of both the static and the local magnetic field within the object to be examined and on the linearity of the gradients used. Conversely, artifacts also increase with increasing field strength,<sup>18</sup> because of, in particular, possible inhomogeneities of  $B_0$ , the local magnetic field, and the type of sequence used.

In the present ultra-high-field MRI study a 7.1 T scanner was used to investigate the potential utility of this technology for imaging the anterior segment in phakic eyes of different species. Special attention was paid to quantification of lens placement and geometry, in particular the axial and equatorial lens diameter, contour length, and lens volume in relation to the sulcus-sulcus or angle-angle plane as a basis for future accommodation studies. The influence of tissue heating, reproducibility, and SNR are discussed quantitatively. Additionally, ultrasound- and 7.1 T MRI-based lens thickness (LT) determinations in monkey eyes were compared.

### METHODS

The study was approved by the ethics committees of the University of Rostock and the University of Nijmegen. All animal experiments were performed in compliance with the ARVO Statement for the Use of Animals in Ophthalmic and Vision Research.

### Animals

The study involved pig, rabbit, human, and monkey eyes. White New Zealand rabbits were acquired from approved vendors in accordance with the requirements of the Animal Welfare Act. Pig eyes were obtained from the local slaughterhouse. Enucleated eyes from rabbits ( $n = 5$ , aged 3.5 years) and pig ( $n = 1$ , aged 6 months) were assessed

From the <sup>1</sup>Institute for Diagnostic Radiology and Neuroradiology, University of Greifswald, Greifswald, Germany; <sup>2</sup>Institute for Biomedical Engineering and <sup>3</sup>Department of Ophthalmology, University of Rostock, Rostock, Germany; <sup>4</sup>AMO Groningen BV, Groningen, The Netherlands; and <sup>5</sup>Department of Ophthalmology, University Medical Center Groningen, University of Groningen, Groningen, The Netherlands.

Supported in part by the DFG (Transregio 37, Micro- and Nanosystems in Medicine—Reconstruction of Biological Functions), KiiAkk REMEDIS, and SenterNovem Dutch Grant IS043081.

Submitted for publication November 5, 2009; revised February 17, April 29, and June 24, 2010; accepted July 16, 2010.

Disclosure: S. Langner, None; H. Martin, None; T. Terwee, None; S.A. Koopmans, None; P.C. Krüger, None; N. Hosten, None; K.P. Schmitz, None; R.F. Guthoff, None; O. Stachs, None

Corresponding author: Oliver Stachs, Department of Ophthalmology, University of Rostock, Doberaner Straße 140, D-18057 Rostock, Germany; oliver.stachs@med.uni-rostock.de.

using the MRI techniques described below. In addition, one phakic human donor eye (aged 40 years) and monkey eyes (phakic  $n = 3$ , pseudophakic  $n = 1$ , aged 10 years) underwent micro-MRI assessment <24 hours after enucleation without any invasive manipulation of the eyes investigated. Before MRI on monkey eyes, LT was measured using A-scan ultrasonography (US; Sonomed A5500; Sonomed, Inc., Lake Success, NY). The ultrasound device was set to a sound velocity of  $1548 \text{ ms}^{-1}$ . LT measurements were converted to actual distances using a sound velocity of  $1641 \text{ ms}^{-1}$ .

### MRI Ex Vivo

Micro-MRI images were acquired using an ultra-high-field MR scanner (7.1 T ClinScan; Bruker Bioscan GmbH, Ettlingen, Germany). Instrument specifications are summarized in Table 1. All eyes investigated were imaged using a phased array transmit-and-receive surface coil with two channels and two coil elements for each channel. The eye to be examined was placed at room temperature on a gauze cushion within the coil. The gauze cushion was supported by a foam pad to minimize unintended motion. The examination protocol consisted of  $T_2$ -weighted turbo spin echo (T2w TSE) sequences. For ex vivo imaging, a FoV of  $40 \times 40 \text{ mm}$  with a matrix size of  $512 \times 512$  pixels was used. The other imaging parameters were TR 3300 ms and TE 75 ms with a turbo factor (TF) of 7. Twenty-two slices with no gap between the slices were acquired, and the slice thickness was  $700 \mu\text{m}$ . The acquisition time was 8:16 minutes. T2w images were acquired in three anatomic planes. To define these planes, localizing sequences were orientated perpendicular and parallel to the center of the ciliary body. Before acquiring the anatomic sequences, color-coded gradient field maps were measured (Fig. 1) to monitor magnetic field inhomogeneities within the FoV. If gradient field mapping revealed severe inhomogeneities, additional shim procedures were performed.

### MRI In Vivo

In vivo measurements on rabbits were performed under general anesthesia. The animals were placed in a supine position inside the scanner. If necessary, the head was stabilized on both sides within the animal bed using additional foam pads. The coil was placed over the eye at a distance of 1 mm, which was kept constant by a small foam pad. The coil was then affixed to the animal bed with adhesive tape. After acquiring localizing sequences parallel and perpendicular to the level of the ciliary body, gradient field mapping was also performed. In comparison to ex vivo imaging, the FoV used for the T2w TSE sequence was  $40 \times 40 \text{ mm}$  with a matrix of  $320 \times 320$  pixels. The other imaging parameters were TR 2420 ms, TE 44 ms, TF 7, 15 slices with a slice thickness of  $700 \mu\text{m}$ , and a gap of 20% between the slices. Acquisition time was 5.12 minutes for each plane with an overall scanning time of 30 minutes. For further analyses, the image data were transferred to a DICOM workstation (eFilm Workstation; Merge Health Care, Milwaukee, WI).

### Tissue Heating

Unlike MRI systems used in routine clinical practice, the MRI scanner used here does not monitor the specific absorption rate. Therefore, the energy deposited due to the gradient systems can only be estimated. To

**TABLE 1.** Specifications for the Ultra-high-field MR Scanner (ClinScan; Bruker Bioscan GmbH)

Field strength: 7.1 T
Diameter of clear bore: >302 mm
Stray field (5 Gauss): $\pm 3 \text{ m}$ axial, $\pm 2 \text{ m}$ radial, actively shielded gradients
Outer/inner diameter: 301.5 mm/200.5 mm
Gradient amplitude: 290 mT/m
Slew rate: 1160 T/m/s
Linearity (130/100 mm DSV): $< \pm 3\%$ / $< \pm 2\%$

DSV, diameter of spherical volume.

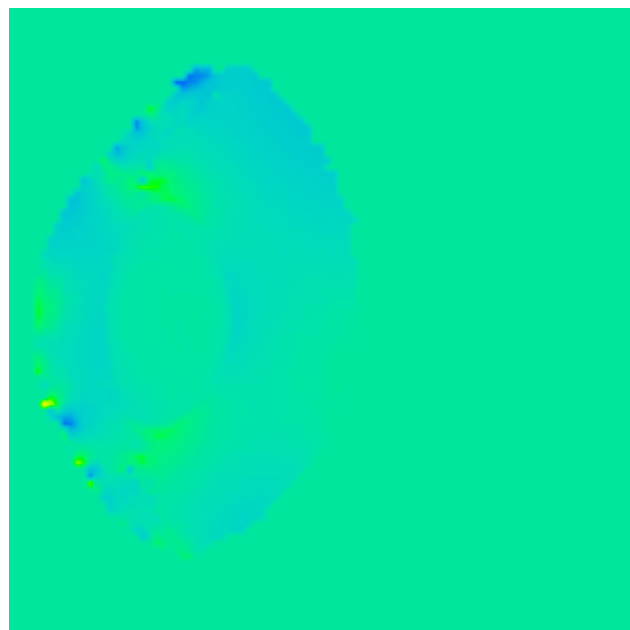


**FIGURE 1.** Color-coded gradient field mapping of a human donor eye. Mean chemical shift was 200 Hz/pixel.

monitor potential tissue heating, a fiber optic thermometer (Fiber Optic Temperature Module in combination with Model 1025 Monitoring & Gating System; SA Instruments, Inc., Stony Brook, NY) was used to obtain representative temperature profiles during ex vivo imaging (temperature range, 0 to  $+70^\circ\text{C}$ ; calibrated accuracy,  $\pm 0.2^\circ\text{C}$ ). The fiber optic probe was inserted into the anterior chamber of a pig eye via a corneal paracentesis. For temperature equalization the enucleated eye was placed on the gauze cushion within the coil 1 hour before scanning. Ambient air temperature was measured simultaneously.

### Reproducibility

To analyze reproducibility, a rabbit eye underwent repeated scanning in vivo. After a first imaging sequence, the animal (white New Zealand rabbit, aged 5 months) was taken out of the scanner, the coil removed, and then refitted on the animal's eye, as described above. Afterward the animal was replaced inside the scanner and reimaged. This procedure was repeated three times. Axial globe cross-sections were selected from the MRI data for each iteration. LT was determined using two different methods: manual marking using the CAD software described below, and analysis of the grayscale distribution along the axial lens diameter followed by lens edge detection using the roots of the second derivation (highest gradient) of the grayscale distribution (Fig. 2).

### Signal-to-Noise Ratio

The SNR of the lens was calculated by defining a region of interest (ROI) around the entire lens in the equatorial plane and another ROI within the surrounding air. Although the ROI of the lens differed for each eye, the surrounding air ROI was constant in size ( $6 \text{ mm}^2$ ).

### Biometry

The CAD-based evaluation method was applied to MR images of eyes from the different species (human, monkey, pig, rabbit). Axial globe cross-sections were selected from the MRI data sets for each eye. These sections were imported into a CAD system (Solid Works 2007; Dassault Systèmes Corp., Concord, MA), and the biometric dimensions were manually marked and calculated (Fig. 3 and Table 2). The aim was to obtain lens dimensions and surface and volume data in relation to the sulcus-sulcus and angle-angle plane. The anterior segment cross-section

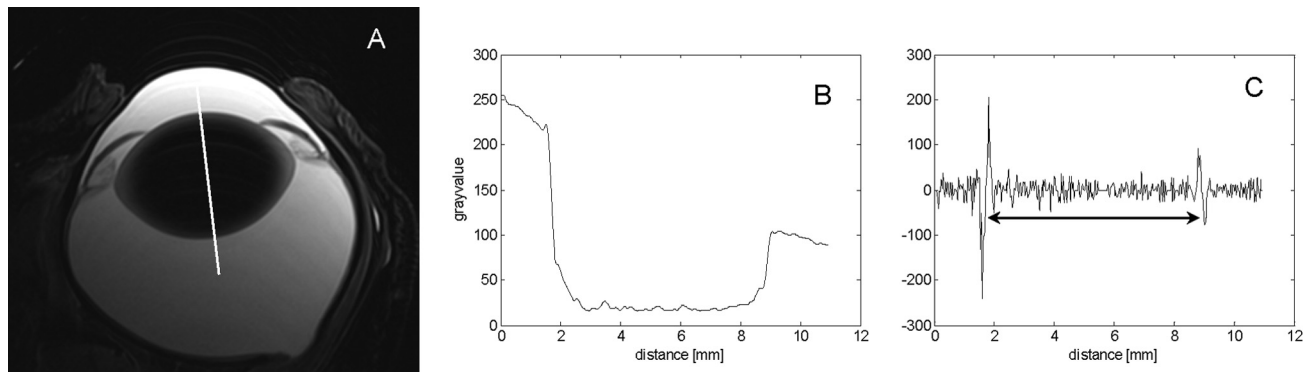


FIGURE 2. Principle of LT determination using an edge detection method. (A) Line along the axial lens diameter; (B) intensity profile; (C) second derivation. Note: the roots of the second derivation are the highest gradients of the intensity profile and were used for edge detection.

presented in Figure 3 defines the various biometric distances. For the determination of lens surface and volume, the lens was constructed as a body of revolution using the digitized contour and the surface, and volume was calculated using the CAD system.

Five individual MRI- and ultrasound-based LT measurements in three different monkey eyes were used for LT comparison. A statistical analysis was performed (SPSS 15.0; SPSS, Chicago, IL). Monkey eye LT data were assessed by the Mann-Whitney *U* test. The level selected for statistical significance was *P* < 0.05.

In one pseudophakic monkey eye, the information provided by the intraocular lens (IOL) manufacturer was compared with MRI-based data. Manufacturer data for the implanted 30 diopter IOL were the following: central thickness 1.32 mm, diameter 6.0 mm, posterior radius of curvature 8.075 mm (spherical), and anterior radius of curvature 8.075 mm (aspherical).

RESULTS

Imaging

Micro-MR imaging for visualization of anatomic anterior segment details was achieved in all eyes examined. For ex vivo imaging, a FoV of 40 × 40 mm with a matrix size of 512 × 512 pixels and a slice thickness of 700 μm yielded in-plane resolution of 80 × 80 μm. For in vivo imaging in rabbits the overall scanning time was approximately 30 minutes with 5.12 minutes for the high-resolution scans for each eye. Matrix size for in vivo imaging was 320 × 320 pixels, resulting in in-plane resolution of 125 × 125 μm (slice thickness, 700 μm).

Tissue Heating, SNR, and Reproducibility

Figure 4 illustrates the placement of the fiber optic probe in the anterior chamber after ex vivo imaging of a pig eye and the

temperature profiles during a 9.18 minute T2w high-resolution scan sequence in the anterior chamber as well as in ambient air. The temperature increase in the anterior chamber was approximately 0.6°C, rising from 23.5 ± 0.1°C to 24.1 ± 0.1°C. Ambient air temperature probe failed to disclose any heating of the room temperature, with a temperature remaining constant at approximately 23.5 ± 0.1°C.

The mean SNR from lens to the surrounding air was found to be 3.20 (pig eye), 2.68 (rabbit eye), 2.89 (human donor eye), and 2.79 (monkey eye) for the ex vivo studies and 4.27 for the in vivo rabbit eye studies.

Data illustrating the reproducibility of biometric distance determinations are presented in Table 3. The LT of an individual rabbit eye was determined by two different methods from three successive scans. A mean value with SD of 7.26 ± 0.13 mm was found for manual thickness determination and 7.21 ± 0.14 mm for the computer-assisted procedure. Both standard deviations are within a range of approximately 2 pixels (in-plane resolution: 125 × 125 μm). Additionally, a difference between these two methods of 0.05 mm was found.

Rabbit and Pig Eye Anatomy—Ex Vivo

Figure 5 shows an axial T<sub>2</sub>-weighted micro-MR image that provides representative examples of pig (Fig. 5A) and rabbit (Fig. 5B) eye anatomy. The eyes show spherical crystalline

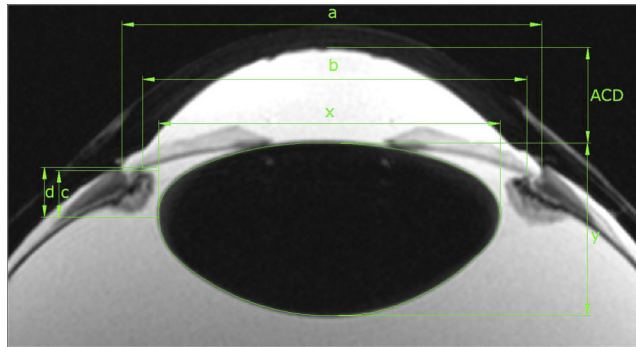


FIGURE 3. Human donor eye with anterior segment biometric distances marked, as presented in Table 2.

TABLE 2. Biometric Distances in the Anterior Segment for a Selected Set of Different Phakic Species

	Human (40 years old)	Monkey (10 years old)	Pig (6 months old)	Rabbit (3.5 years old)
Lens thickness <i>y</i> , mm	4.74	3.82	8.52	8.52
Lens diameter <i>x</i> , mm	9.79	8.69	11.02	12.01
Anterior chamber depth ACD, mm	2.67	2.05	2.67	2.70
Contour length, mm	23.36	20.11	30.52	31.75
Cross-section area, mm <sup>2</sup>	35.7	24.8	71.9	76.24
Sulcus to sulcus <i>a</i> , mm	11.73	9.84	14.48	15.77
Angle to angle <i>b</i> , mm	10.59	9.84	13.38	14.89
Distance <i>c</i> , mm	1.31	0.97	2.03	0.69
Distance <i>d</i> , mm	0.86	0.47	1.29	0.40
Lens volume, mm <sup>3</sup>	230.3	135.1	519.1	584.8
Lens surface, mm <sup>2</sup>	202.1	148.4	317.3	348.5



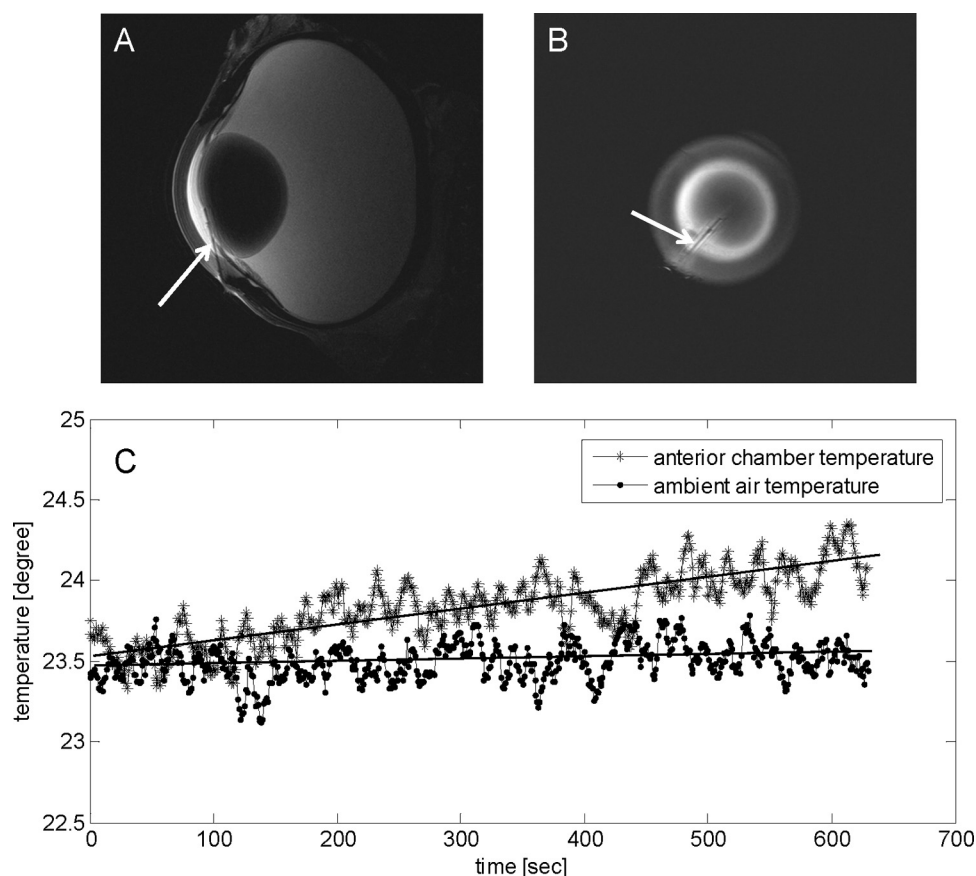


FIGURE 4. (A, B) representative ex vivo MR image of a pig eye with a fiber optic temperature probe placed in the anterior chamber. (C) Ambient air temperature and temperature profile in the anterior chamber of the eye during acquisition of a T2w high-resolution scan.

lenses with pronounced ciliary processes, whereas the ciliary muscle cannot be separated. Zonular fibers or groups cannot be imaged. Lens dimensions and sulcus-sulcus as well as angle-angle distances for two selected eyes (rabbit, pig) are presented in Table 2.

### Primate Eye Anatomy—Ex Vivo

Micro-MR images of a human donor eye (Fig. 6A) aged 40 years and a monkey eye (Fig. 6B) aged 10 years obtained ex vivo are presented in Figure 6. A biometric analysis of the different lens geometries specified in Figure 3 is presented in Table 2. The human lens is slightly larger than the monkey lens. The equatorial lens plane is located more anteriorly in the monkey eye than in the human eye. Single zonular fibers or zonular fiber groups cannot be separated. The ciliary muscle is far more pronounced in monkeys than in humans, and conversely the ciliary processes are more pronounced in humans.

### Micro-MRI versus A-Scan Biometry in Monkey Eyes

Ultrasound- and MRI-based LT determinations in three monkey eyes (aged 10 years) were compared, and the findings are

TABLE 3. LT Determination in Three Successive Rabbit Eye Scans In Vivo Using Two Different Determination Methods (Manual, Computer-Assisted)

Scan	Manual (mm)	Computer-Assisted (mm)	Difference (mm)
1	7.25	7.21	0.04
2	7.39	7.35	0.04
3	7.13	7.07	0.06
Mean $\pm$ SD	7.26 $\pm$ 0.13	7.21 $\pm$ 0.14	0.05

presented in Figure 7 and Table 4. The mean ultrasound-based LTs (sound velocity of  $1641 \text{ ms}^{-1}$ ) are slightly greater than the MRI-based values. No significant differences in LT determinations in monkey eyes were detected between 7.1 T MRI and A-scan US ( $P > 0.05$ , Mann-Whitney  $U$  test).

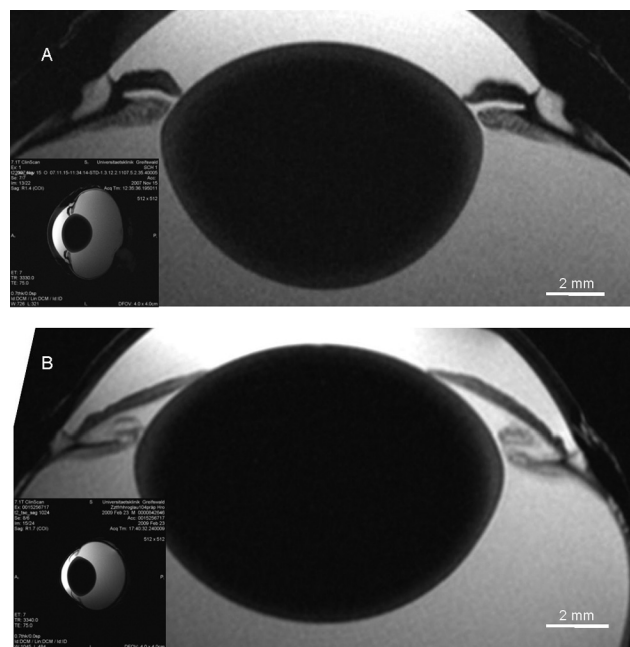
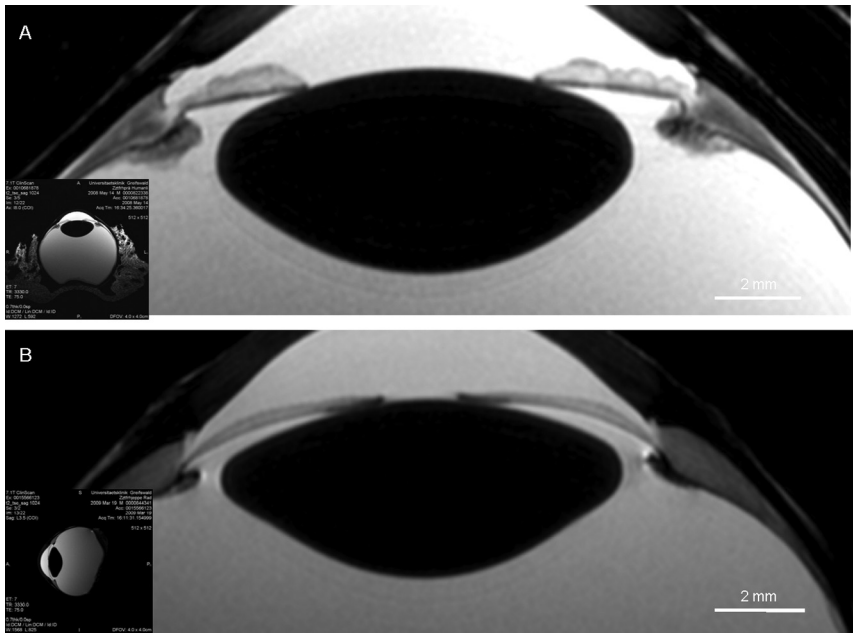


FIGURE 5. Representative micro-MR images of pig eye (A) and rabbit eye (B) anatomy (crystalline lens, ex vivo; FoV,  $40 \times 40 \text{ mm}$ ; matrix size,  $512 \times 512$  pixels).



**FIGURE 6.** Micro-MR images of a human donor eye (A) aged 40 years and a monkey eye (B) aged 10 years (crystalline lens, ex vivo; FoV, 40 × 40 mm; matrix size, 512 × 512 pixels).

**Pseudophakic Monkey Eye**

Figure 8 shows the MR image of a pseudophakic monkey eye, which is overlaid with the IOL manufacturer’s information for central thickness (1.32 mm) and diameter (6.00 mm) as well as posterior and anterior radius of curvature (8.075 mm). It is evident that a circular arc with  $R = 8.075$  mm shows very close alignment with the spherical posterior IOL surface. This is in contrast with the aspherical anterior surface where the central portion shows close alignment, whereas an offset is apparent in the periphery. The anterior capsule can be separated (indicated by an asterisk).

**Phakic Rabbit Eye—In Vivo**

A high-resolution MR ocular image of the crystalline lens of a rabbit obtained in vivo is shown in cross-section in Figure 9. The

findings are comparable with those obtained on ex vivo imaging but with a lower in-plane resolution of 125 × 125 μm.

**DISCUSSION**

This study demonstrates the potential of high-field MRI in an ophthalmology setting for visualizing normal anterior segment anatomy. Unlike other well-established ophthalmological imaging methods, MRI provides true anatomic proportions independent of the optical and absorption characteristics of the ocular tissues. Earlier published in vivo studies<sup>13–15,19–24</sup> using 1.5 T MR imagers have shown an SNR resulting in limited resolution. Surface coils of various configurations have been used in the past, for example, to investigate anatomy,<sup>19</sup> intraocular metastases,<sup>20</sup> ocular and orbital lesions,<sup>21</sup> as well as extraocular muscles.<sup>22</sup> MRI has been used to observe the relationship between ciliary muscle activity and lens response,<sup>10,13,23,24</sup> changes in lens volume during accommodation,<sup>14</sup> and cataractous lens changes.<sup>25</sup> Richdale et al.<sup>17</sup> have developed protocols that optimize contrast, resolution, and scan time for three-dimensional imaging of the human eye in vivo using a 7 T scanner. The Miyake-Apple technique, video analysis, and MRI have been used to investigate anterior segment structures after surgical manipulation of postmortem eyes.<sup>15</sup> Recent accommodation studies using MRI are quite rare compared with those using optical and ultrasound technologies.

One drawback with the studies cited above is the limited SNR with 1.5 T MR systems. Although 1.5 T MR scanners provide good contrast, spatial resolution, and detail, they offer inferior SNR when compared with ultra-high-field MRI. The MRI method developed by Strenk et al.<sup>10,23,24,26</sup> for in vivo imaging of the anterior segment provides an FoV of 40 × 40 mm and in-plane resolution of 156 × 156 μm<sup>26</sup> and 78 × 78

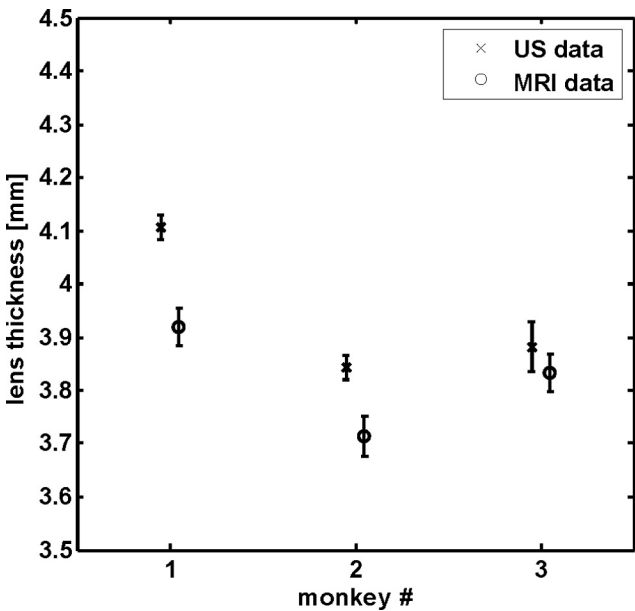


**FIGURE 7.** LT (mm) in 3 monkey eyes determined by A-scan US and micro-MRI.

**TABLE 4.** Monkey Eye LT Measured by MRI and A-Scan US

Monkey Number	LT <sub>MRI</sub> (mm)	LT <sub>US</sub> (mm)	Difference (mm)
1	3.92 ± 0.04	4.11 ± 0.02	0.19
2	3.71 ± 0.03	3.84 ± 0.02	0.13
3	3.82 ± 0.04	3.88 ± 0.05	0.05

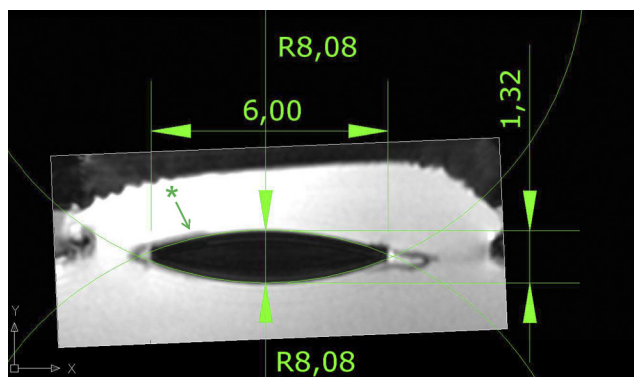


**FIGURE 8.** Micro-MR image of a pseudophakic monkey eye overlaid with the IOL manufacturer's optic data (central thickness, 1.32 mm; diameter, 6 mm). The posterior circular arc with a radius of curvature of 8.075 mm is closely aligned with the spherical IOL surface, by contrast with the anterior aspherical surface.

$\mu\text{m}$ ,<sup>23</sup> respectively. Using 7.1 T and T2w TSE sequences, it was possible to achieve in-plane resolution of  $80 \times 80 \mu\text{m}$  ex vivo and  $125 \times 125 \mu\text{m}$  in vivo when imaging the anterior and posterior segments of the eye.

Consequently, although the theoretical in-plane resolution for this study using 7.1 T is almost comparable with that in the 1.5 T studies conducted by Strenk, there is greater SNR. Therefore, the image information with 7.1 T appears far more detailed. The anterior segment cross-sections presented in Figures 5 and 6 confirm this conclusion. In addition, there was no alteration of image quality because of eye movements, micro-saccades, for example, when ex vivo imaging was performed. Similarly, artifacts due to eye movements were also not an issue when in vivo imaging was performed under general anesthesia. Ex vivo imaging not only allows the coil to be placed closer to the surface of the cornea, but also reduces artifacts caused by the lid, a complication encountered in previous in vivo studies of the human eye<sup>17</sup>.

Compared with laser techniques and Scheimpflug imaging, micro-MRI is not superior and offers no improvement for determining axial LT or imaging the central radius of curvature. However, the advantage of high-field MRI technology, which has the capability of 3D image and data analysis, is that it reveals overall lens geometry in relation to ciliary body configuration and lens volume. A full set of biometric data is shown in Table 2 for the different species to illustrate the potential of ultra-high-field MRI. This is applicable for both crystalline lenses as well as intraocular lenses (although data on the latter are not presented here). This demonstrates the advantage of MRI over optical and ultrasound methods. Again, the capability to acquire the entire lens shape rather than part of it may yield more precise knowledge about lens volume and the principal lens dimensions, including radius of curvature. For instance, overall lens dimensions in relation to sulcus-sulcus distance are important in regard to new IOL implants designed to correct presbyopia.

Ultrasound and MRI-based LT determinations were compared to identify the correlation between these two methods. A systematic difference (mean,  $120 \mu\text{m}$ ) was detected, with higher values for US (Fig. 7; Table 4). This 3% offset may be due to a variety of factors, such as sound velocity for US, ultrasound transducer alignment, or tilt of MRI cross-sections. However, the systematic offset is more suggestive of a systematic error, and any future study must include a larger set of samples to permit detailed analysis of this phenomenon. The SD on ultrasound-based LT determination

is comparable to that based on MRI data ( $\text{SD}_{\text{US}} = 0.030 \text{ mm}$ ,  $\text{SD}_{\text{MRI}} = 0.035 \text{ mm}$ ). No significant differences were detected between 7.1 T MRI and A-scan US in terms of LT determinations in monkey eyes ( $P > 0.05$ , Mann-Whitney *U* test). It can therefore be concluded that a micro-MRI-based quantitative analysis of anterior segment dimensions is comparable to that based on A-scan US.

Use of color-coded gradient field maps enabled the visualization of the homogeneity of the local magnetic field within the eye. Together with the linearity of the magnetic gradients used for imaging, this is the major prerequisite for obtaining true anatomic proportions without optical distortion. This has been demonstrated clearly in practice by comparing the IOL manufacturer's optic data with the MR image of a pseudophakic monkey eye (Fig. 8). In-plane distances are identical, and a circular arc with the exact radius of curvature is closely aligned with the posterior spherical surface of the IOL. This analysis confirms the absence of relevant distortion artifacts inside the MR images. Coincidentally, micro-MRI offers astonishingly high repeatability, as demonstrated by LT determinations. Repeated scanning on the same eye resulted in a SD of approximately 0.14 mm, equivalent to  $<2$  pixels in plane.

One limitation of ultra-high-field MRI with surface coils<sup>18</sup> is the signal drop-off from the surface of the coil to the center of the vitreous body. The same limitation was described by Richdale et al.<sup>17</sup> and is also known from previous studies at 1.5 T. For imaging the anterior segments of the eye, surface coils are preferable and provide excellent SNR.

Increasing the strength of the static magnetic field and the gradients could theoretically lead to radio frequency (RF)-induced heating of tissue, with the attendant potential for altering contrast. RF-induced temperature changes might alter T1 and T2 values of the tissue investigated. Temperature was therefore monitored ex vivo in a pig eye during a T2w TSE sequence, revealing a slight temperature increase, as assessed with a fiber optic probe placed in the anterior chamber. The probe is immune to electromagnetic- and radio frequency-induced interferences, and temperature measured with this probe is caused only by the RF-induced tissue heating of the probe itself. A temperature increase in the anterior chamber of  $0.6^\circ\text{C}$  was found during a 9.18 minute T2w high-resolution scan sequence. These temperature changes observed in this study did not lead either to cross-contrast changes or to geometrical distortions, and this was demonstrated by the results of the reproducibility studies. These findings are supported by the work of Richdale et al.,<sup>17</sup> who did not observe changes in T1 values during imaging of the human eye in vivo at 7 T.

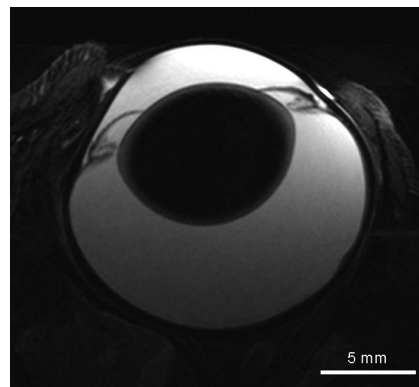


**FIGURE 9.** High-resolution MR images of rabbit eye anatomy in vivo (FoV,  $40 \times 40 \text{ mm}$ ; matrix size,  $320 \times 320$  pixels).



The published in vivo studies cited above, in combination with the ex vivo and in vivo animal and donor eye studies presented here, demonstrate the future potential of high-field MRI for enhancing biomechanical understanding and the biometric evaluation of the crystalline lens and of artificial intraocular lenses. At present, particularly for humans, access to this technology is still limited because of the small tube diameter; however, new high-field systems are opening fresh horizons in intraocular imaging. In the future, ultra-high-resolution MRI will become an extremely useful modality that permits visualization of the relationship between ciliary muscle activity and lens response, including the circumlental space. The present study lends weight to the body of opinion that micro-MRI technology should be introduced into anterior segment imaging and justifies the investment of further efforts to establish this technology in experimental and clinical ophthalmology. This novel approach to exploring the anterior segment of the eye yields high-resolution images without optical distortion and overcomes many of the major limitations that are a feature of other quantitative imaging modalities.

### Acknowledgments

The authors acknowledge the contribution of Tim Wokrina (Bruker BioSpin, Germany) for providing the fiber optic thermometer and Helga Krentz for statistical advice.

### References

1. Wolffsohn JS, Peterson RC. Anterior ophthalmic imaging. *Clin Exp Optom*. 2006;89:205-214.
2. Foster FS, Pavlin CJ, Harasiewicz KA, Christopher DA, Turnbull DH. Advances in ultrasound biomicroscopy. *Ultrasound Med Biol*. 2000;26:1-27.
3. Fink W. Refractive correction method for digital charge-coupled device-recorded Scheimpflug photographs by means of ray tracing. *J Biomed Opt*. 2005;10:024003.
4. Linnola RJ, Findl O, Hermann B, et al. Intraocular lens-capsular bag imaging with ultrahigh-resolution optical coherence tomography pseudophakic human autopsy eyes. *J Cataract Refract Surg*. 2005;31:818-823.
5. Trick GL, Edwards PA, Desai U, Morton PE, Latif Z, Berkowitz BA. MRI retinovascular studies in humans: research in patients with diabetes. *NMR Biomed*. 2008;21:1003-1012.
6. Chen JJ, Wang Q, Zhang HY, et al. In vivo quantification of T-1, T-2, and apparent diffusion coefficient in the mouse retina at 11.74T. *Magn Reson Med*. 2008;59:731-738.
7. Braun RD, Gadianu M, Vistisen KS, Roberts RL, Berkowitz BA. Manganese-enhanced MRI of human choroidal melanoma xenografts. *Invest Ophthalmol Vis Sci*. 2007;48:963-967.
8. Li SK, Jeong EK, Hastings MS. Magnetic resonance imaging study of current and ion delivery into the eye during transscleral and transcorneal iontophoresis. *Invest Ophthalmol Vis Sci*. 2004;45:1224-1231.
9. Ito Y, Berkowitz BA. MR studies of retinal oxygenation. *Vis Res*. 2001;41:1307-1311.
10. Strenk SA, Strenk LM, Semmlow JL. High resolution MRI study of circumlental space in the aging eye. *J Refract Surg*. 2000;16:S659-S660.
11. Derevanik NL, Wilson CA, Berkowitz BA, Mahlow J, Vinos SA. Blood-retinal barrier (BRB) breakdown in diabetic rabbits assessed by electron microscopic immunocytochemistry and magnetic resonance imaging (MRI). *Invest Ophthalmol Vis Sci*. 1996;37:4430.
12. Georgouli T, James T, Tanner S, et al. High-resolution microscopy coil MR-Eye. *Eye*. 2008;22:994-996.
13. Koretz JE, Strenk SA, Strenk LM, Semmlow JL. Scheimpflug and high-resolution magnetic resonance imaging of the anterior segment: a comparative study. *J Opt Soc Am A Opt Image Sci Vis*. 2004;21:346-354.
14. Hermans EA, Pouwels PJW, Dubbelman M, Kuijter JPA, van der Heijde RGL, Heethaar RM. Constant volume of the human lens and decrease in surface area of the capsular bag during accommodation: an MRI and Scheimpflug study. *Invest Ophthalmol Vis Sci*. 2009;50:281-289.
15. Pereira FA, Werner L, Milverton EJ, Coroneo MT. Miyake-Apple posterior video analysis/photographic technique. *J Cataract Refract Surg*. 2009;35:577-587.
16. Poley BJ, Lindstrom RL, Samuelson TW, Schulze R Jr. Intraocular pressure reduction after phacoemulsification with intraocular lens implantation in glaucomatous and nonglaucomatous eyes: evaluation of a causal relationship between the natural lens and open-angle glaucoma. *J Cataract Refract Surg*. 2009;35:1946-1955.
17. Richdale K, Wassenaar P, Teal BK, et al. 7 Tesla MR imaging of the human eye in vivo. *J Magn Reson Imaging*. 2009;30:924-932.
18. Ladd ME. High-field-strength magnetic resonance: potential and limits. *Top Magn Reson Imaging*. 2007;18:139-152.
19. Ettl A, Zwrtek K, Daxer A, Salomonowitz E. Anatomy of the orbital apex and cavernous sinus on high-resolution magnetic resonance images. *Surv Ophthalmol*. 2000;44:303-323.
20. Lemke AJ, Hosten N, Wiegel T, et al. Intraocular metastases: differential diagnosis from uveal melanomas with high resolution MRI using a surface coil. *Eur Radiol*. 2001;11:2593-2601.
21. Bilaniuk LT, Schenck JF, Zimmerman RA, et al. Ocular and orbital lesions: surface coil MR imaging. *Radiology*. 1985;156:669-674.
22. Ohnishi T, Noguchi S, Maurakami N, et al. Extraocular-muscles in Graves ophthalmopathy: usefulness of T2 relaxation-time measurements. *Radiology*. 1994;190:857-862.
23. Strenk SA, Strenk LM, Guo S. Magnetic resonance imaging of aging, accommodating, phakic, and pseudophakic ciliary muscle diameters. *J Cataract Refract Surg*. 2006;32:1792-1798.
24. Strenk SA, Strenk LM, Semmlow JL, DeMarco JK. Magnetic resonance imaging study of the effects of age and accommodation on the human lens cross-sectional area. *Invest Ophthalmol Vis Sci*. 2004;45:539-545.
25. Lizak MJ, Datiles MB, Aletras AH, Kador PF, Balaban RS. MRI of the human eye using magnetization transfer contrast enhancement. *Invest Ophthalmol Vis Sci*. 2000;41:3878-3881.
26. Strenk SA, Semmlow JL, Strenk LM, Munoz P, Gronlund-Jacob J, DeMarco JK. Age-related changes in human ciliary muscle and lens: a magnetic resonance imaging study. *Invest Ophthalmol Vis Sci*. 1999;40:1162-1169.